Xian *et al. Journal of Nanobiotechnology* (2025) 23:247
https://doi.org/10.1186/s12951-025-03322-0

Journal of Nanobiotechnology

RESEARCH Open Access

Reduction of colitis in mice by chemically programmed supramolecular nanoassemblies of vitamin–lipid conjugates

Shiyun Xian[1,2†], Fanchao Meng[1,2†], Xiaona Chen[3], Liqing Zhu[4*] and Hangxiang Wang[1,2*]

Abstract

Inflammatory bowel disease (IBD) is a relapsing disorder characterized by uncontrolled chronic inflammation of the gastrointestinal tract, posing a significant therapeutic challenge owing to the limited efficacy and undesirable side effects of current therapeutic options. A key pathological hallmark of IBD is the excessive production of reactive oxygen species (ROS). Hence, therapeutic strategies aimed at reducing ROS levels are promising for relieving these inflammatory conditions. Vitamin C—a natural nutrient for the human body—is well known for its potent antioxidant effects. However, the clinical development of vitamin C as a therapeutic drug has been hindered by its poor stability, rapid metabolism, and inadequate tissue accumulation. Herein, we report that the bioavailability of vitamin C can be enhanced by chemically reprogramming it with a small panel of long-chain fatty acids that aid in the aqueous self-assembly of the resulting drug conjugates to create self-deliverable nanoassemblies, enhancing their inflammation disease–oriented delivery and cellular uptake. In mice with dextran sulfate sodium–induced colitis, the optimal vitamin C–lipid nanoassemblies preferentially accumulated in inflamed colonic tissues following systemic administration and substantially ameliorated disease severity. We extended this strategy to incorporate the clinically approved glucocorticoid budesonide into the vitamin C nanosystem, facilitating a synergistic combination. In the chronic colitis model, the combination treatment reduced inflammation without compromising global immunity. Mechanistically, the treatment modulated the intestinal inflammatory microenvironment and altered the immune cell landscape, partly through regulation of the gut microbiome. Given its anticipated negligible side effects, this novel nanoassembly platform leveraging small-molecule lipidation may become a promising therapeutic for treating various inflammatory diseases.

Keywords Inflammatory bowel disease, Vitamin C, Budesonide, Lipid conjugate, Self-assembly

†Shiyun Xian and Fanchao Meng contributed equally to this work.

*Correspondence:
Liqing Zhu
wzzhuliqing@126.com
Hangxiang Wang
wanghx@zju.edu.cn
[1]Jinan Microecological Biomedicine Shandong Laboratory, Jinan, Shandong Province 250118, P. R. China
[2]The First Affiliated Hospital, NHC Key Laboratory of Combined Multi-Organ Transplantation, Collaborative Innovation Center for Diagnosis and Treatment of Infectious Diseases, State Key Laboratory for Diagnosis and Treatment of Infectious Diseases, Zhejiang University School of Medicine, Hangzhou, Zhejiang Province 310003, P. R. China
[3]Department of Medical Oncology, Sir Run Run Shaw Hospital, Zhejiang University School of Medicine, Hangzhou, Zhejiang Province 310003, P. R. China
[4]Department of Clinical Laboratory, Peking University Cancer Hospital and Institute, Beijing, P. R. China

Introduction

Inflammatory bowel disease (IBD), including ulcerative colitis and Crohn's disease, is a complex and relapsing disorder characterized by uncontrolled chronic inflammation of the gastrointestinal tract, resulting in intestinal damage [1]. The global burden of IBD has increased drastically, afflicting over 3.5 million individuals worldwide [2]. Notably, chronic and long-standing inflammation in patients with IBD has led to an increased risk of developing colorectal cancer and other severe complications [3, 4]. Furthermore, current therapeutic options for IBDs, such as immunosuppressants, biological therapies, and antibiotics [5], only provide limited efficacy, with a large proportion of patients experiencing undesired adverse effects. The necessity for lifelong medication further exacerbates the risk of infections and malignancies, highlighting the critical need for alternative treatments for IBD with negligible side effects.

Oxidative stress is closely associated with the pathogenesis of various inflammatory conditions, such as IBD [6, 7]. Excessive production of reactive oxygen species (ROS) has been implicated in the development of colitis [8], suggesting that the depletion of ROS using with anti-ROS therapies could offer therapeutic benefits. Vitamin C (V_C), also known as ascorbic acid, is a potent natural antioxidant and an essential nutrient for human health [9, 10]. Despite its potential, the clinical development of V_C as a drug for effective IBD treatment is hindered by its poor stability, rapid clearance and metabolism from the body, and insufficient accumulation in inflamed tissues [11, 12]. We hypothesize that a nanotherapeutic strategy could enhance the targeting and accumulation of antioxidant agents at sites of inflammation. However, creating therapeutic nanoparticles from the hydrophilic and unstable V_C molecule while maintaining its pharmacologic efficacy has remained a significant technical challenge.

To overcome these challenges, we aimed to develop a straightforward yet broadly applicable approach for reusing V_C, a molecule with suboptimal drug–like properties, as an inflammation-protective nanotherapeutic. Supramolecular nanotherapeutics, constructed through noncovalent interactions between molecular components, offer superior therapeutic outcomes compared to their free counterparts in treating various diseases [13]. By integrating active compounds into these nanostructures *via* physical encapsulation or covalent conjugation, their intrinsic biological characteristics are preserved [14, 15]. For example, the attachment of lipid moieties such as squalene to drugs results in prodrug amphiphiles that can assemble into colloidally stable nanoaggregates [13]. Additionally, natural polyunsaturated fatty acids (PUFAs) facilitate the rational design of therapeutics into self-deliverable nanoplatforms with enhanced pharmacokinetics and pharmacological efficacy [16, 17]. In addition to therapeutically active drugs, only PUFAs, which are both abundant in the human body and beneficial for the health, are released upon systemic administration [18]. Inspired by the "PUFAylation" technology previously applied to anticancer agents [19], we aim to broaden the use of PUFAs as assembly motifs for nanoassemblies that deliver antioxidant agents for treating intestinal injuries.

We covalently attached V_C to a series of fatty acids to validate our approach. Fatty acids are hydrophobic, and V_C is hydrophilic. Thus, when two molecules are ligated, they form amphiphilic lipid conjugates that are capable of self-assembling into nanostructures in an aqueous solution (Fig. 1A). A panel of V_C amphiphiles was synthesized through esterification, which spontaneously formed nanoparticles (Fig. 1B). Screening for stability and ROS-scavenging capacity led to the identification of linoleic acid (LA)–derived nanoassemblies as a promising nanotherapeutic candidate. These engineered nanoassemblies preferentially targeted sites of intestinal inflammation and effectively neutralized ROS production induced by dextran sulfate sodium (DSS) [20]. Furthermore, the integration of the clinically approved glucocorticoid drug budesonide (Bud) into the V_C nanosystem facilitated a combination treatment approach for inflammatory diseases. In murine models of acute and chronic colitis, the optimized V_C or combination nanoassemblies successfully alleviated intestinal injury from the onset of colitis. Our study highlights the potential of lipid conjugation and nanoassembly to convert V_C into a therapeutic agent for inflammatory diseases.

Results

Rational design and self-assembly of V_C–lipid conjugates

V_C is chemically unstable and rapidly eliminated from the body, hindering its accumulation and therapeutic efficacy in inflamed tissues [11]. To overcome these limitations, we engineered a series of V_C–lipid conjugates by tethering hydrophobic lipid moieties to the V_C molecule, enhancing its amphiphilicity. We selected a wide range of fatty acids, including saturated fatty acids such as heptanoic acid (HA) and decanoic acid (DA), monounsaturated fatty acids such as oleic acid (OA), and polyunsaturated fatty acids such as LA, linolenic acid, eicosapentaenoic acid (EPA), and docosahexaenoic acid (DHA) for this purpose. The synthesis of seven distinct V_C–lipid derivatives, namely V_CHA, V_CDA, V_COA, V_CLA, V_CLNA, V_CEPA, and V_CDHA, was achieved through the esterification of V_C's hydroxyl group with the respective fatty acids catalyzed by lipase. The successful synthesis of these conjugates was validated by ^{1}H NMR spectroscopy (Figure S1–S7), and their purities were

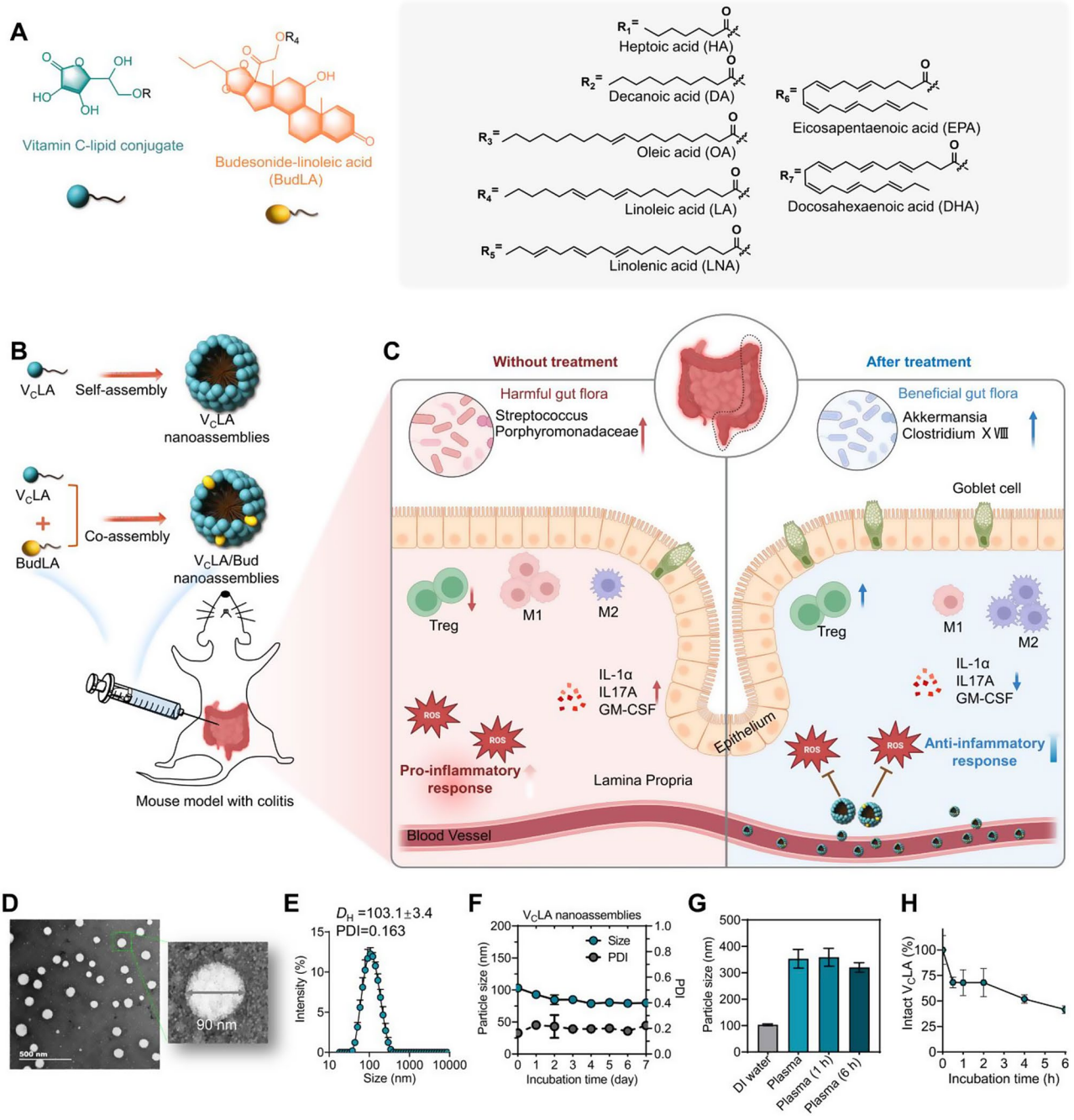

Fig. 1 Rational design and characterization of lipid–vitamin C (V_C) conjugates and their aqueous nanoassemblies (NAs) for colitis treatment in animal models. (**A**) Chemical structures of fatty acid–conjugated V_C and budesonide (Bud) derivatives. (**B**) Schematic illustration of self-assembly of the resultant prodrugs into V_CLA or V_CLA/Bud nanoassemblies in aqueous solutions. (**C**) These nanoassemblies are designed to target and accumulate in the inflamed colon upon intraperitoneal administration, where they specifically modulate the inflammatory microenvironment. The therapeutic effects include the elimination of reactive oxygen species (ROS), alteration of macrophage subtypes, regulation of T cells, reduction of proinflammatory cytokines, and modulation of the gut microbiome. (**D**) Representative TEM images of V_CLA nanoassemblies. (**E**) Hydrodynamic size distribution and polydispersity index of V_CLA nanoassemblies determined by dynamic light scattering (DLS). (**F**) Stability assessment of V_C nanoassemblies stored at 4 °C over one week ($n = 3$). (**G**) Particle size changes of V_CLA nanoassemblies after incubation with mouse plasma ($n = 3$). (**H**) Analysis of the integrity of the V_CLA conjugates following incubation with rat serum, as determined by reverse-phase high-performance liquid chromatography (RP-HPLC) ($n = 3$). Data are presented as mean ± standard deviation (s.d.)

confirmed by reversed-phase high-performance liquid chromatography (RP-HPLC; Figure S8).

The resultant V_C–lipid derivatives exhibited poor water solubility but showed good miscibility with polar organic solvents such as dimethyl sulfoxide (DMSO). Employing a standard nanoprecipitation protocol, wherein DMSO-dissolved V_C–lipid conjugates were added to water, followed by the removal of DMSO through dialysis, led to the formation of water-dispersible nanoassemblies. These nanoassemblies were characterized by their transparent solutions and further analyzed using transmission electron microscopy (TEM), which revealed their nearly spherical morphologies (Fig. 1D and S9A). Dynamic light scattering (DLS) analysis indicated that the particle sizes of these seven different V_C nanoassemblies varied largely, ranging from 100 to 500 nm (Fig. 1E and S9B). Among them, the nanoassemblies derived from V_CLA exhibited narrow size distributions and are stable colloidal suspensions (Fig. 1F and S9C). Upon incubation with mouse plasma, the particle size of V_CLA nanoassemblies increased due to protein corona formation but remained stable over a 6-h incubation period (Fig. 1G). Furthermore, the chemical stability of V_CLA nanoassemblies was maintained throughout the incubation period (Fig. 1H). These findings underscore the potential of V_C–lipid conjugates as promising candidates for preparing injectable formulations and enhancing their stability, paving their way for the application in therapeutic interventions.

Evaluation of the antioxidant activity of V_C nanoassemblies in vitro

The antioxidant potential of V_C–lipid nanoassemblies was assessed to determine if they retained the ROS-scavenging capacity of natural V_C. We evaluated the neutralizing capacity of these nanoparticles against hydrogen peroxide (H_2O_2), a key endogenous ROS involved in inflammatory responses. Employing the 2,2′-azino-bis (3-ethylbenzo-thiazoline-6-sulfonic acid) (ABTS+•) assay, we observed that the lipid derivatization of V_C and its subsequent nanoaggregation did not compromise the antioxidant activity, as evidenced by the strong radical-scavenging capability comparable to that of free V_C (Fig. 2A). Additionally, the 2-phenyl-4,4,5,5-tetramethylimidazoline-1-oxyl 3-oxide (PTIO•) scavenging assay for in vitro ROS reaffirmed that the anti-ROS potential of V_C–lipid nanoassemblies remained largely intact despite modifying the V_C hydroxyl group with hydrophobic fatty acids (Fig. 2B).

The conjugation of fatty acids to V_C increases its lipophilicity, which enhances the transport of V_C derivatives and related nanoassemblies across cellular membranes, thereby amplifying their intracellular antioxidant activity [21]. The intracellular ROS-scavenging ability of V_C nanoassemblies was examined using the DCFH-DA fluorescence probe. Lipopolysaccharide (LPS) can simulate the polarization of mouse macrophage RAW264.7 cells, accompanied by ROS overproduction. Upon exposure to LPS (1 μg/mL), the cells exhibited morphological changes (Figure S10B) and emitted a robust green fluorescence signal indicative of intracellular ROS generation (Fig. 2C). Pretreatment with free V_C attenuated the fluorescence intensity in LPS-stimulated RAW264.7 cells. Notably, V_CLA nanoassemblies effectively diminished the fluorescence signal (Fig. 2C), suggesting their capacity to mitigate ROS production in RAW264.7 cells. The ability of V_CLA nanoassemblies to protect RAW264.7 cells from oxidative stress–induced death was further assessed. Calcein-AM/propidium iodide (PI) staining revealed that V_CLA nanoassemblies increased the proportion of live cells (green fluorescence), whereas free V_C exhibited a moderate protective effect, likely due to limited cellular uptake (Fig. 2D). Consistent results were obtained from the CCK-8 viability assay (Fig. 2F), indicating the efficacy of V_CLA nanoassemblies in safeguarding RAW264.7 cells against ROS-mediated cytotoxicity. Moreover, the protective efficacy of V_CLA nanoassemblies was validated in a normal human colon mucosal epithelial cell line, NCM460, through live/dead cell staining and a CCK-8 assay, confirming their ability to alleviate oxidative stress in the cells (Fig. 2E and G). In vitro ROS-scavenging capacity and favorable stability led to the selection of V_CLA nanoassemblies for further investigations.

In vivo ROS-scavenging capacity and nanoassembly accumulation in the inflamed colon

IBD is a complex disorder characterized by persistent inflammation in the gastrointestinal tract, particularly in the ileum, rectum, and colon [22]. Sustained generation of ROS is a key factor in the pathogenesis of IBD [23]. Given the promising antioxidant and cytoprotective properties of V_CLA nanoassemblies observed in vitro, we sought to evaluate their potential to mitigate ROS overproduction in a DSS-induced colitis mouse model (experimental design is illustrated in Fig. 3A). To monitor ROS levels in vivo, we administered the near-infrared fluorescence (NIRF) probe L-012 to DSS-induced colitis mice. Remarkably, the ROS levels in mice treated with V_CLA nanoassemblies were considerably lower than those in mice treated with saline or free V_C (Fig. 3B), highlighting the ROS-scavenging capacity of the nanoassemblies.

The effective delivery of therapeutic nanoparticles to sites of intestinal inflammation is crucial for the successful treatment of colon diseases. The elevated ROS levels at inflamed sites can disrupt endothelial junctions, facilitating the accumulation of nanosized particles in the damaged colon [24]. We investigated the localization of nanoparticles in the colons of healthy versus DSS-induced colitis mice (Fig. 3C). After intraperitoneal

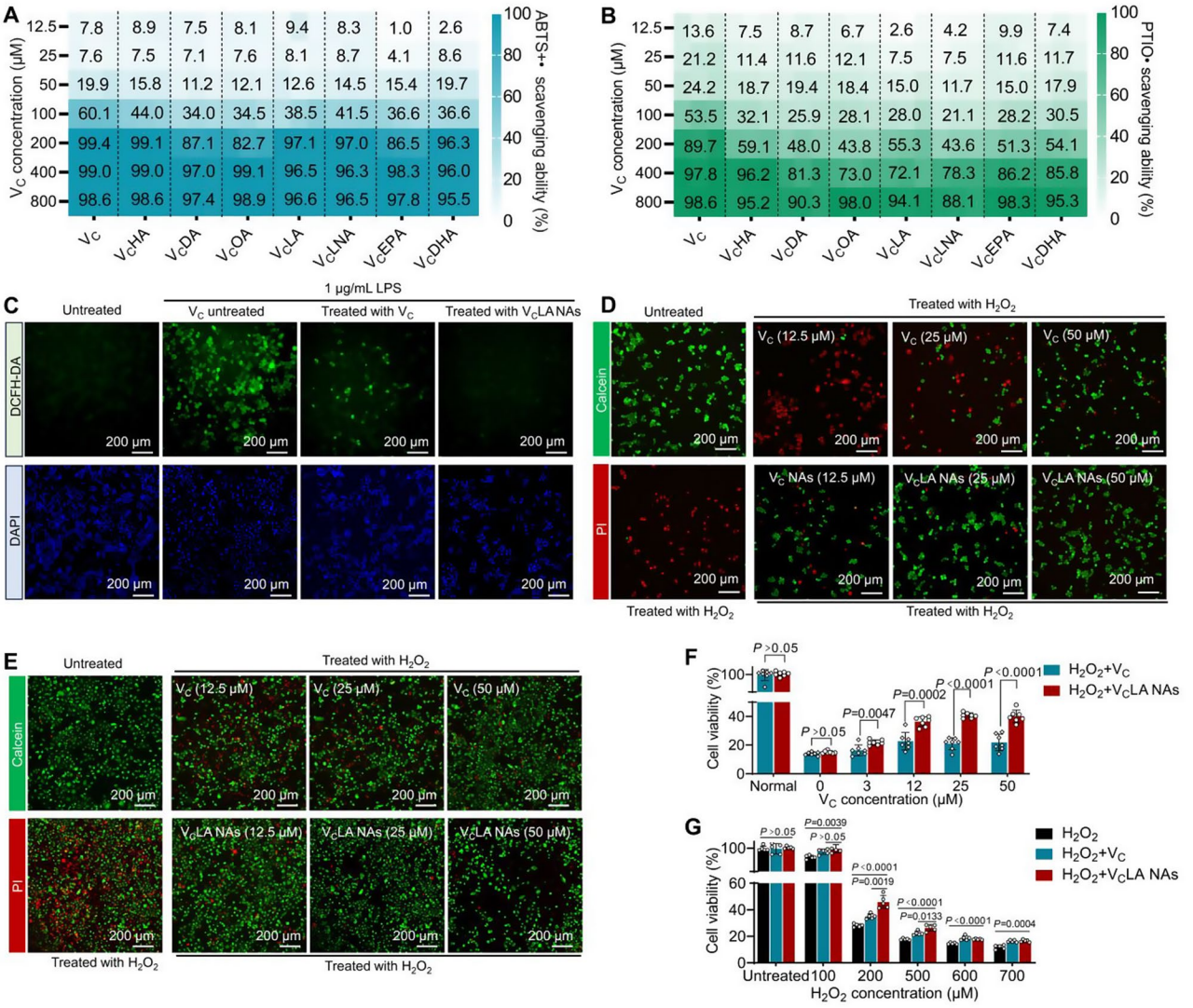

Fig. 2 In vitro assessment of the antioxidant capacity of V_C nanoassemblies (NAs). (**A** and **B**) The antioxidant capacity of a series of V_C nanoassemblies and free V_C was evaluated using PTIO· and ABTS+· assays. The numbers in the figure represent the average percentages of three experimental results at the same V_C concentration. (**C**) Representative fluorescence images depict the ROS levels in RAW264.7 cells treated with various agents (PBS, LPS, LPS + V_C, and LPS + V_CLA nanoassemblies) for 24 h. DCFH-DA was employed to visualize ROS production (green) and Hoechst staining was used to visualize nuclei (blue). (**D**) Live/dead cell assay using calcein-AM/PI staining assessed the protective effect of V_CLA nanoassemblies on RAW264.7 cells. V_CLA nanoassemblies demonstrated enhanced protective effects against cell death compared to free V_C. (**E**) Cell viability of RAW264.7 coincubated with 600 μM H_2O_2 and increasing concentration of free V_C or V_CLA nanoassemblies, as measured by the CCK-8 assay. (**F**) Fluorescence microscopy images for dead/live cell staining of NCM460 cells. Following drug treatments, cells were costained with calcein-AM (green, live cells) and propidium iodide (red, dead cells) ($n = 3$). (**G**) Cell viability of NCM460 cells after treatment with various concentrations of free V_C or V_CLA nanoassemblies ($n = 3$). Data are presented as mean ± standard deviation (s.d.)

injection of the NIRF dye (i.e., Cy5.5-LA)-labeled V_CLA nanoassemblies, major organs were harvested and analyzed using NIRF imaging. Notably, the colons of colitis mice exhibited stronger NIRF signals from V_CLA nanoassemblies than colons of healthy mice, indicating preferential nanoparticle accumulation at the inflamed sites (Fig. 3D). Quantitative analysis confirmed a threefold increase in fluorescence intensity in the colons of DSS-treated mice compared to healthy controls (Fig. 3E). Confocal laser scanning microscopy further validated the abundant accumulation of nanoparticles in the colons of colitis-infected mice (Fig. 3F and G). Overall, our findings demonstrate that systemically administered V_CLA nanoassemblies can effectively localize to inflamed intestinal tissues and reduce ROS levels in a mouse model of colitis. Furthermore, the preferential delivery and ROS-scavenging capacity suggest the potential of V_CLA nanoassemblies as a promising therapeutic strategy for the treatment of IBD.

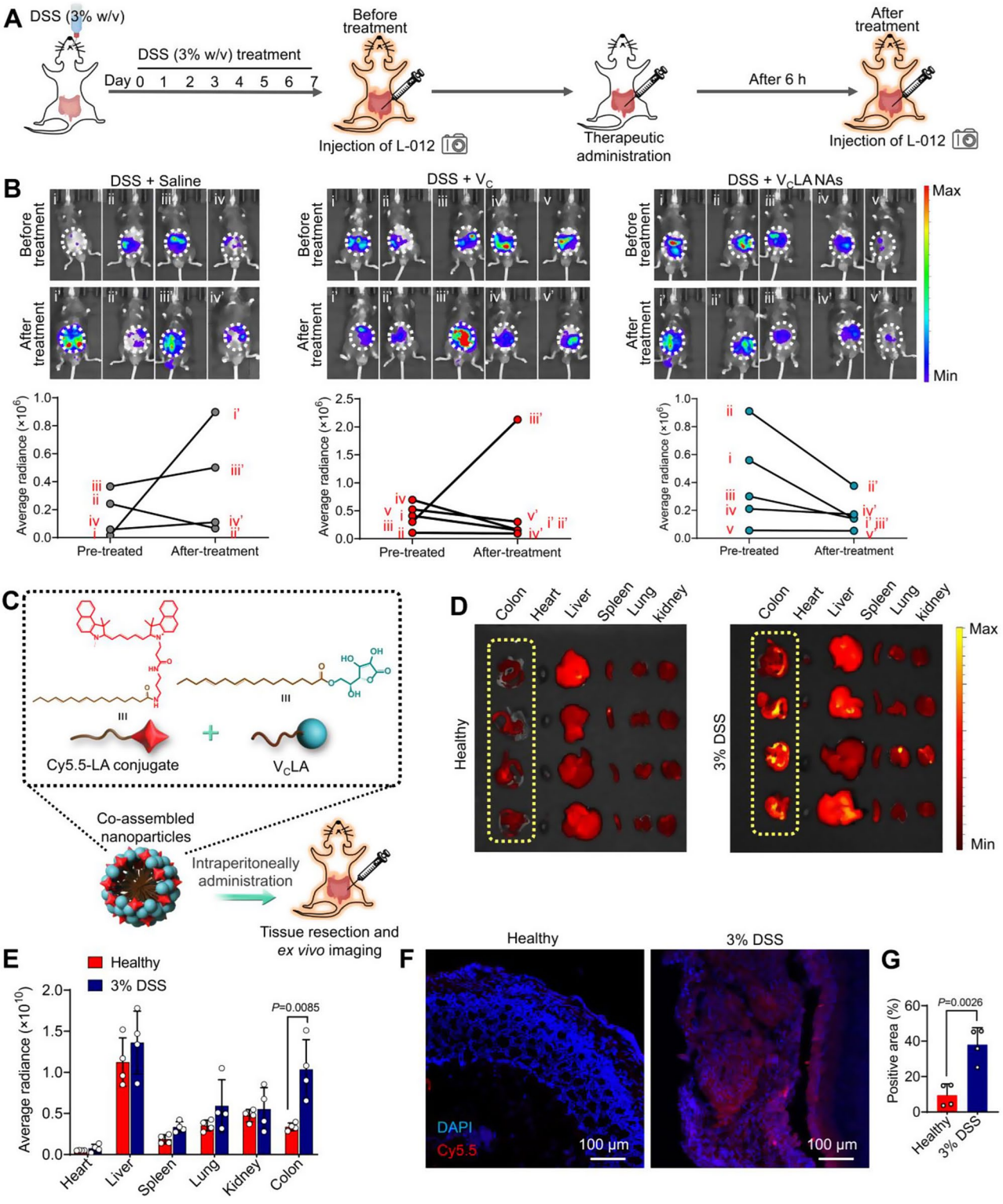

Fig. 3 (See legend on next page.)

Amelioration of acute colitis by V_CLA nanoassemblies in a DSS-induced mouse model

To evaluate the translational potential of V_CLA nanoassemblies for IBD treatment, we conducted in vivo efficacy studies using an acute colitis mouse model. The well-established DSS-induced colitis model was employed, where six-week-old C57BL/6 mice were exposed to 3% DSS in drinking water for 7 days to induce acute

(See figure on previous page.)

Fig. 3 In vivo ROS-scavenging capacity and accumulation of V_CLA nanoassemblies (NAs) in the inflamed colon. (**A**) Schematic representation of the experimental protocol for evaluating reactive oxygen species (ROS) levels in vivo ($n = 4–5$). (**B**) Near-infrared fluorescence (NIRF) images of ROS levels before and after treatment with free V_C or V_CLA nanoassemblies. C57BL/6 mice were administered water containing 3% dextran sulfate sodium (DSS) to induce colitis. The rise or decline in ROS levels in each mouse was determined before and after treatment using a ROS-specific probe. (**C**) Schematic representation of the protocol for investigating the localization of nanoparticles in the colons. After intraperitoneal injection of Cy5.5-labeled V_CLA nanoassemblies, tissue biodistribution was assessed in healthy mice and DSS-induced colitis mice using NIRF imaging ($n = 4$). Ex vivo NIRF imaging (**D**) and quantitative analysis (**E**) of V_CLA nanoassemblies quantity in major organs postadministration ($n = 4$). (**F**) Representative confocal microscopy images of tissue sections showed that V_CLA nanoassemblies (red) tend to target the inflamed colon. (**G**) Quantification of the red fluorescence intensity in confocal images ($n = 4$). Data are presented as mean ± standard deviation (s.d.)

colitis [4, 25], mimicking key aspects of IBD in humans (scheme of animal experiment illustrated in Fig. 4A). The drug treatment was initiated accordingly, and V_CLA formulated in liposomes (termed lipo V_CLA) was also included for comparison. The onset of colitis was characterized by severe bloody diarrhea and loose stools by day 6, with mice treated with saline or free V_C exhibiting pronounced colitis symptoms (Fig. 4B). A significant reduction in body weight, nearly 20%, was observed in these groups (Fig. 4C). In contrast, mice receiving V_CLA liposomes or nanoassemblies demonstrated a less pronounced decrease in body weight (Fig. 4C). The severity of bloody diarrhea was further assessed using an occult blood test paper on day 6. Additionally, the Disease Activity Index (DAI) was calculated based on weight fluctuation, stool consistency, and stool occult blood (Table S1). The scoring results indicated that V_CLA nanoassemblies treatment effectively mitigated the progression of colitis (Fig. 4D and E).

At the end of the study, mice were euthanized, and their spleens and colons were harvested for histopathological analysis. Splenomegaly, commonly observed in chronic inflammation diseases, including IBD, was evident in mice with colitis. Notably, the administration of V_CLA nanoassemblies significantly ameliorated splenomegaly (Fig. 4F and G). Morphometric analysis revealed that the colons of mice with colitis who received saline and free V_C were shorter than those treated with V_CLA liposomes or nanoassemblies (Fig. 4H and I). Furthermore, histopathological examination using hematoxylin and eosin (H&E) staining showed that colons from both V_CLA-treated groups closely resembled those of healthy mice. In contrast, saline- or free V_C-treated mouse colons presented typical features of colitis, including loss of epithelial crypts, inflammation, and ulceration (Fig. 4J). Masson's staining indicated that V_CLA nanoassemblies could decrease aberrant collagen proliferation (Fig. 4K). Furthermore, periodic acid–Schiff (PAS) staining revealed that after V_CLA nanoassembly treatment, colons preserved the integrity of goblet cells, which is essential for mucus secretion and maintaining physiological functions (Fig. 4L). Although free V_C demonstrated strong antioxidant activity in vitro, it failed to exert a protective effect in the colitis mouse model, with mice receiving V_C treatment developing a similar degree of DSS-induced colitis as control saline–treated mice. In contrast to free V_C, self-assembled V_CLA nanoparticles exhibited a protective role in DSS-induced colitis, underscoring their potential as a therapeutic strategy for IBD.

Coassembled lipid nanotherapy for alleviating chronic inflammation in a mouse model of DSS-induced colitis

Chronic colitis poses significant therapeutic challenges and increases the risk of colorectal cancer, necessitating the development of safe and effective new treatments [26]. In this study, we explored the integration of budesonide (Bud), a clinically approved glucocorticoid drug for inflammatory diseases, into the self-assembled V_CLA nanosystem to combat chronic colitis [27, 28]. The conjugation of Bud with unsaturated fatty acid (e.g., LA) resulted in a novel prodrug entity, BudLA (Fig. 1A), demonstrating self-assembling capacity in an aqueous solution [29]. We investigated whether BudLA could coassemble with V_CLA nanoparticles to form a transparent codelivery therapeutic solution, termed V_CLA/Bud nanoassemblies (Fig. 5A and B). V_CLA/Bud nanoassemblies exhibited a hydrodynamic diameter of ~ 120 nm and remained stable at room temperature for over a month, as determined by DLS analysis (Fig. 5C and D).

Armed with the coassembling nanotherapy, we evaluated its efficacy against chronic colitis onset using a well-established mouse model by administering 3.5% DSS in drinking water for 5 days in two cycles [30] (Fig. 5E). In this model, mice treated with saline or BudLA nanoassemblies exhibited severe bloody diarrhea (Fig. 5E). Administration of either V_CLA or V_CLA/Bud nanoassemblies provided adequate protection against DSS-induced chronic colitis, as evidenced by restored body weights and no mouse mortality during the study, whereas four out of six mice treated with saline succumbed to colitis onset (Fig. 5F and G). Additional assessments included measuring bloody diarrhea and calculating the DAI, which further confirmed the superior therapeutic efficacy of the V_CLA/Bud nanoassemblies over monotherapies (Fig. 5H and I). Notably, the combination treatment inhibited splenomegaly and maintained normal colon length in DSS-induced colitis mice, indicating a favorable prognosis (Fig. 5J–L). Histopathological evaluations of colon tissues demonstrated that treatment with codelivered nanoassemblies preserved intact epitheliums,

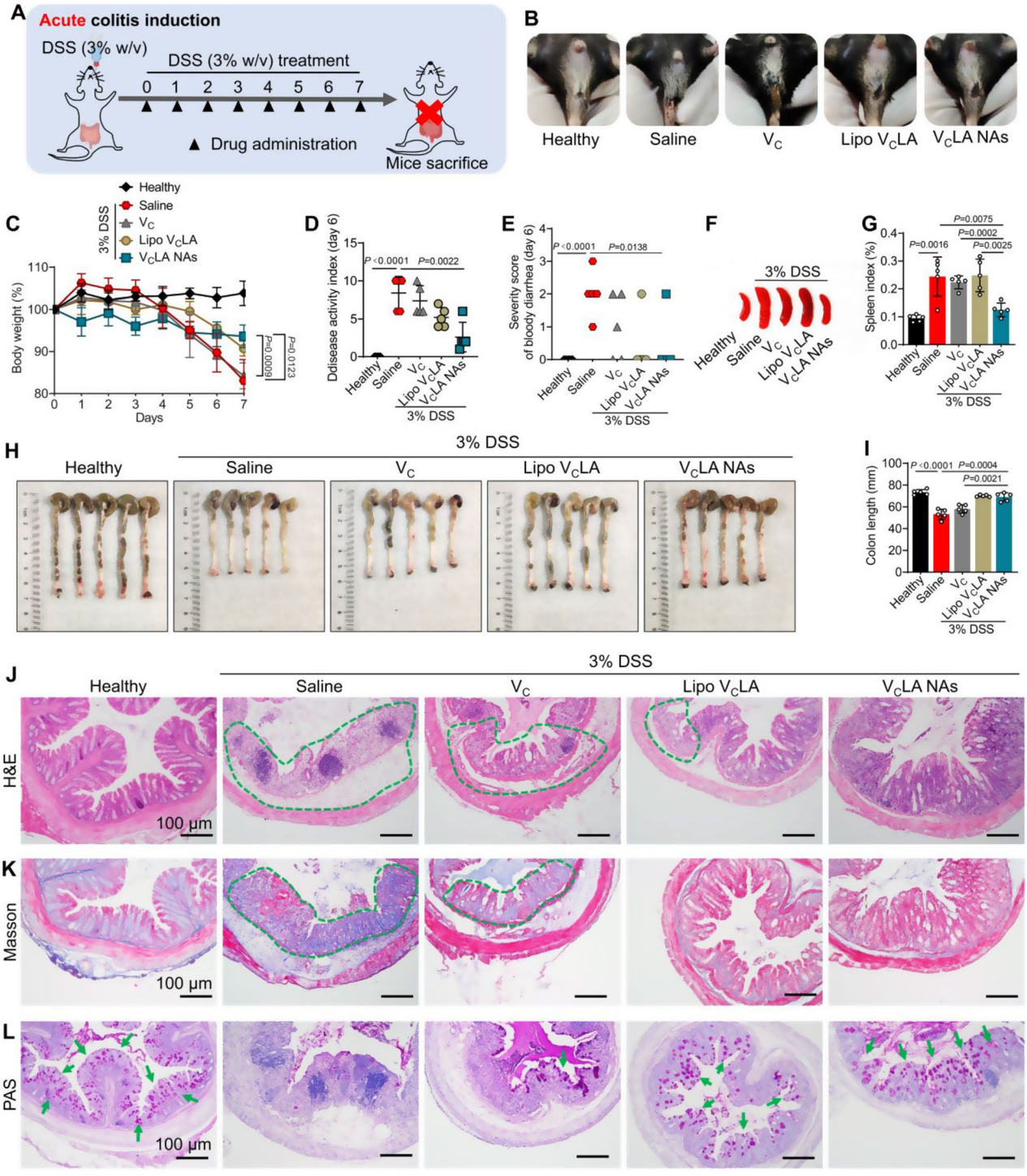

Fig. 4 Alleviation of acute colitis in a DSS-induced mouse model by V_CLA nanoassemblies (NAs). (**A**) Schematic representation of the induction of acute colitis in C57BL/6 mice using 3% dextran sulfate sodium (DSS). (**B**) Representative photographs of the anal region from each treatment group. Apart from the healthy group, other mice received intraperitoneal treatment with saline, free V_C, V_CLA nanoassemblies, and V_CLA liposomes (Lipo V_CLA) at a dosage of 10 mg/kg (V_C equivalent) daily ($n = 5$). (**C**) Weight fluctuations of mice relative to the first day ($n = 5$). (**D**) Disease Activity Index (DAI) and (**E**) severity of bloody diarrhea were scored on day 6 ($n = 5$). (**F**) Representative photographs and (**G**) quantified spleen index of spleens dissected on the last day. (**H**) Photographs of all colons and (**I**) statistical analysis of colon lengths ($n = 5$). (**J**) Hematoxylin and eosin (H&E) staining, (**K**) Masson's staining, and (**L**) periodic acid–Schiff (PAS) staining of colon sections. Green dotted circles in H&E and Masson's staining indicate abnormal colon morphology and deposited collagen, respectively. Green arrows indicate goblet cells. Data are presented as mean ± standard deviation (s.d.)

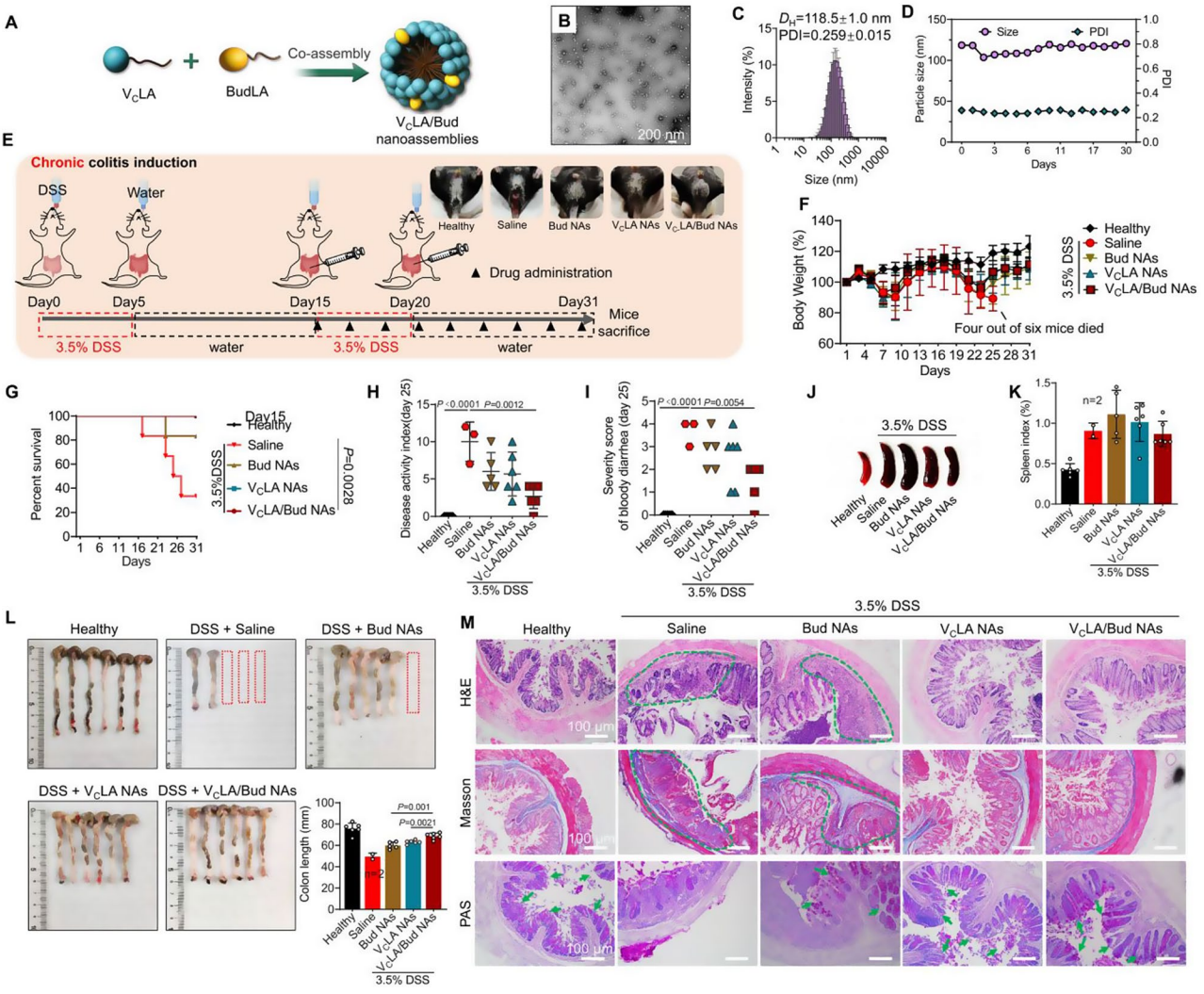

Fig. 5 Coassembled lipid nanoassemblies (NAs) alleviate chronic inflammation in DSS-induced colitis mice. (**A**) Schematic representation of V_CLA/Bud coassembled nanoparticles with a 50:1 mass ratio of V_C and Bud. (**B**) Representative TEM images showcasing the morphology of coassembled nanoparticles. (**C**) Particle size and (**D**) particle stability of V_CLA/Bud nanoassemblies were assessed by DLS. (**E**) Schematic outline of the induction protocol for colitis and drug treatment regimen, accompanied by representative photographs of the mouse anal region from five groups. Concurrent with 3.5% DSS administration in drinking water, mice were intraperitoneally injected with saline, BudLA nanoassemblies (Bud NAs), V_CLA nanoassemblies, or V_CLA/Bud nanoassemblies apart from the healthy group every other day from day 15 to day 30 ($n = 5$). (**F**) Body weight variation compared to the first day ($n = 2$–6). (**G**) Survival rate curve of each group was monitored for 31 days. (**H**) Disease Activity Index (DAI) and (**I**) severity of bloody diarrhea were evaluated ($n = 3$–6). (**J**) Representative photographs and (**K**) quantified spleen index of spleens dissected on day 31. (**L**) Photographs of all colons under the same scale and statistical analysis of colon lengths after fecal removal. (**M**) Hematoxylin and eosin (H&E) staining, Masson's staining, and periodic acid–Schiff (PAS) staining of colon sections were used to assess morphology, collagen deposition, and goblet cells, respectively. Green dotted circles in H&E and Masson's staining indicate abnormal colon morphology and deposited collagen, respectively. Green arrows indicate goblet cells. Data are presented as mean ± standard deviation (s.d.)

well-defined crypt structures, reduced collagen deposition, and maintained goblet cell integrity during colitis (Fig. 5M). Thus, treatment with V_CLA/Bud nanotherapy after the onset of inflammation effectively controlled colitis and attenuated intestinal damage in animal models.

Rewiring the intestinal inflammatory microenvironment in DSS-induced colitis mice

Emerging studies underscore the imbalance between proinflammatory and anti-inflammatory cytokines as a key driver in IBD progression [31]. IL-1 α is reported to be upregulated in the inflamed intestinal track, exerting proinflammatory effects by disrupting the gut microbial ecosystem, leading to mucosal disease, barrier dysfunction, and tissue damage [32] (Fig. 6A). Moreover,

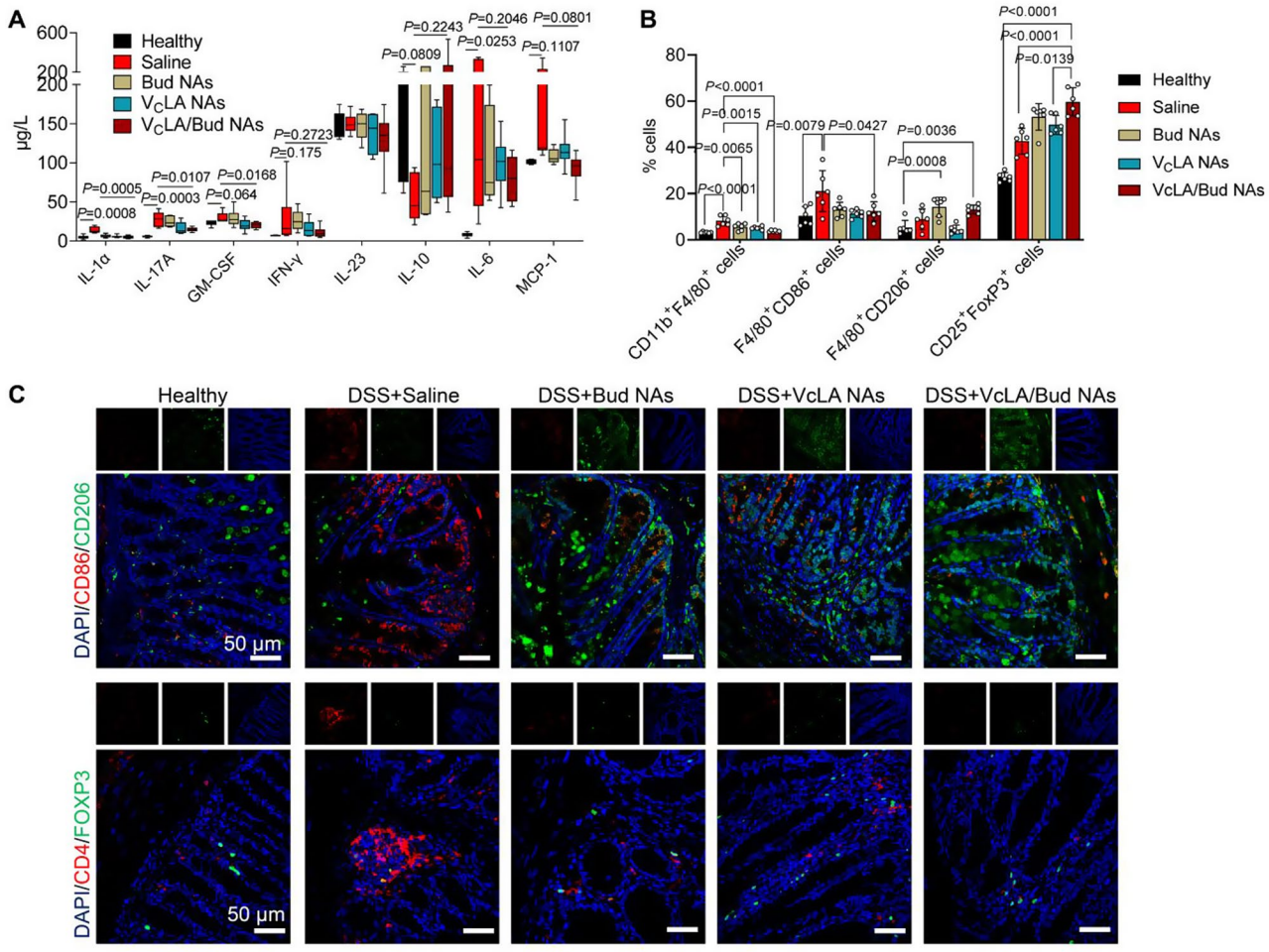

Fig. 6 V_CLA/Bud nanoassemblies alleviated the inflammatory microenvironment in DSS-induced colitis mice. (**A**) Levels of IL-1α, IL-17 A, GM-CSF, IFN-γ, IL-23, IL-10, IL-6, and MCP-1 in the serum of mice after cessation of different treatments ($n=6$). (**B**) Total macrophage cells (gating as $CD11b^+F4/80^+$ cells), M1-subtype type cells (gating as $F4/80^+CD86^+$ cells), M2-subtype cells (gating as $F4/80^+CD206^+$ cells) and Treg cells (gating as $CD25^+FoxP3^+$ cells) in colon tissues were analyzed by flow cytometry ($n=6$). (**C**) Representative immunofluorescence images of the M1-, M2-like macrophages and Tregs in colon tissue. Data are presented as mean ± standard deviation (s.d.)

IL-17 A, secreted by T helper cell 17 (Th17), is overexpressed in the colonic lamina propria (cLP) during IBD onset [33]. We choose serum to evaluate systemic inflammatory responses, which are crucial for determining the overall immune modulation induced by the treatment. Our results demonstrated that DSS treatment led to an increase in IL-1α and IL-17 A, but V_CLA/Bud nanoassembly treatment notably downregulated both cytokines in serum, reflecting the alleviation of intestinal inflammation (Fig. 6A). Specifically, we evaluated the production of granulocyte-macrophage colony–stimulating factor (GM-CSF), primarily secreted by activated T cells, B cells, or epithelial cells. During IBD development, GM-CSF is considered an instigator of inflammation [34]. Surprisingly, our results revealed a reduction in GM-CSF secretion after administering V_CLA/Bud nanoassemblies, facilitating the swift recovery from colitis (Fig. 6A). These data highlight the potential of V_CLA/Bud nanoassemblies to modulate the intestinal inflammatory microenvironment, particularly by regulating proinflammatory cytokines IL-1α, IL-17 A, and GM-CSF levels.

The critical role of macrophages in host immune functions prompted our investigation into macrophage alterations within the cLP in a DSS-induced colitis mouse model [35]. Flow cytometry analysis indicated an elevated percentage of colonic macrophages in DSS-colitis mice due to severe inflammation. Intriguingly, V_CLA/Bud nanoassemblies substantially reduced the proportion of macrophages (Fig. 6B and S11). The results revealed a significant upregulation of the proinflammatory M1-subtype cell population in the inflamed colon. In contrast, the M1-subtype cell population in the cLP post-treatment with V_CLA/Bud nanoassemblies closely resembled that of the healthy colon (Fig. 6B). Furthermore, M2-subtype cells were significantly upregulated in V_CLA/Bud nanoassemblies-treated tissues compared to normal

and DSS-treated tissues. Tregs, a critical immunosuppressive cell to protect tissues against excessive immune responses [36], was highly enriched in the colon of mice treated with V_CLA/Bud nanoassemblies (Fig. 6B). Additionally, the immunofluorescence staining of tissue sections indicated a similar alteration of M1-, M2-subtype cell and Tregs populations in the cLP in the nanoparticle-treated mice than in the saline group (Fig. 6C).

Modulation of the gut microbiome by V_CLA/Bud nanoassemblies in mice with colitis

The gut microbiome plays a pivotal role in the pathogenesis of IBD, influencing disease onset and progression [37, 38]. We further explored the impact of V_CLA/Bud nanoassemblies on the gut microbiota of mice subjected to different treatment regimens (Fig. 7A). 16 S ribosomal RNA gene sequencing revealed no significant changes in community α-diversity (Shannon and Simpson indices) between V_CLA/Bud-treated mice and saline-treated controls (Fig. 7B). However, partial least squares discriminant analysis (PLS-DA) and nonmetric multidimensional scaling (NMDS) analysis demonstrated a distinct shift in community clustering patterns in β-diversity in mice treated with 3% DSS compared to healthy controls (Fig. 7C and D). Further analysis of community barplots and heatmaps revealed significant alterations in gut microbiota distributions following DSS treatment compared to healthy mice. In contrast, mice receiving

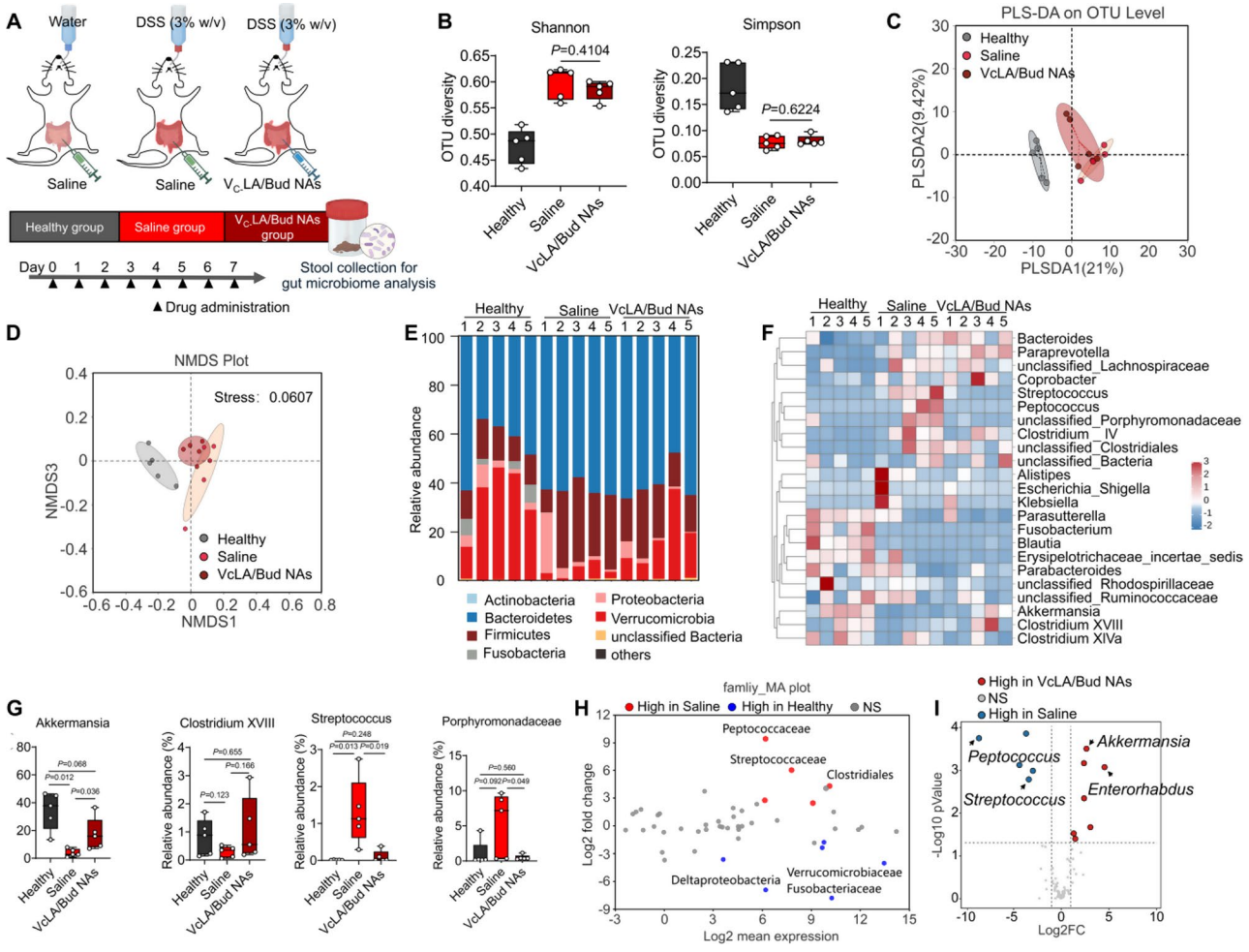

Fig. 7 Alteration of gut microbiome following treatment with V_CLA/Bud nanoassemblies (NAs). (**A**) Schematic illustration of the experimental protocol for dextran sulfate sodium (DSS) administration and V_CLA/Bud nanoassembly treatment for gut microbiome analysis ($n = 5$). (**B**) Assessment of microbial α-diversity using Shannon and Simpson indices, indicating the impact of V_CLA/Bud nanoassembly treatment on gut microbial diversity ($n = 5$). (**C**-**D**) Microbial β-diversity using (**C**) partial least squares discriminant analysis (PLS-DA) and (**D**) nonmetric multidimensional scaling (NMDS) analysis at the end of the treatment period ($n = 5$). Each point represents an individual mouse. (**E**) Barplot depicting the relative abundance of gut microbiota at the phylum level, illustrating shifts in microbial composition following treatments. (**F**) Heatmap showcasing the relative abundance of gut microbiota at the species level (displayed as normalized Z-score). (**G**) Comparative analysis of the relative abundance of selected taxa, underscoring changes in specific microbial populations post-treatment ($n = 5$). (**H**-**I**) High-density microbial community profiles at the (**H**) family and (**I**) species taxonomic levels in the healthy and saline groups, demonstrating the baseline and treatment-induced variations in gut microbiota. Data are presented as mean ± standard deviation (s.d.)

V_CLA/Bud treatment exhibited gut microbiota profiles that were more similar to those of healthy mice (Fig. 7E and **F**). Notably, treatment with V_CLA/Bud nanoassemblies substantially increased the relative abundance of beneficial microbiota, such as *Akkermansia* and *Clostridium* XVIII, along with a significant reduction in harmful *Streptococcus* populations (Fig. 7G). *Akkermansia* is known for maintaining a healthy mucosal barrier in the gut [39–41], while *Clostridium* XVIII is recognized as a butyrate producer, essential for providing energy to colonocytes in the intestinal tract [42].

Additionally, mice exposed to 3% DSS exhibited distinct alterations in gut microflora composition at both the phylum and species levels compared to those receiving standard water (Fig. 7H and I). This change was characterized by an elevated abundance of specific detrimental microbial taxa, such as *Peptococcaceae* and *Streptococcaceae*, underscoring the successful induction of the colitis model. Remarkably, fecal samples from the group subjected to V_CLA/Bud nanoassemblies treatment demonstrated a discernible resurgence of beneficial microbial consortia, with notable enrichment of *Akkermansia* species. Linear discriminant analysis effect size (LEfSe) analysis further identified specific enrichments in the DSS- and V_CLA/Bud-treated groups. Based on cladogram and linear discriminant analysis scores, *Bacteroides* and *Prevotellaceae* exhibited a significant increase in mice receiving V_CLA/Bud nanoassemblies. In contrast, *Enterobacteriaceae*, *Streptococcaceae*, *Klebsiella*, and *Peptococcaceae*, which impact the prognosis of intestinal inflammation, were enriched in DSS-treated mice (Figures S12A and B).

Safety profile assessment of V_CLA/Bud nanoassemblies

Intrigued by the exceptional anti-inflammatory efficacy against two colitis animal models, we conducted a comprehensive toxicity assessment of V_CLA/Bud nanoassemblies. Initially, RAW264.7 and NCM460 cells were treated with increasing concentrations of nanoassemblies, and cell viability was measured after 24–48 h. Notably, no cytotoxicity was detected in both cell lines, even at a high concentration of 100 μM (V_C equivalence) (Figure S10A). Subsequently, the safety profiles of V_CLA/Bud nanoassemblies were examined in healthy ICR mice. The administration dose was increased to twice the therapeutic dose in the chronic colitis model. Throughout the observation period until day 12, post the first injection, mice exhibited healthy and consistent weight growth in each group (Fig. 8A). Additionally, no variations in organ index were observed, as determined by organ weights (Fig. 8B). We further collected peripheral blood for routine blood and blood biochemical analyses. The blood test results indicated no significant differences in any indicator between the treatment groups (Fig. 8C-E). Histopathological examination of organ tissues revealed no remarkable morphological changes (Fig. 8F). These findings highlight the favorable biocompatibility of V_C/Bud nanoassemblies. Importantly, the biosafety assessment of these nanoassemblies provides theoretical support for their practical application in IBD and encourages further steps toward clinical translation.

Discussion

The pathogenesis of IBD is complex and influenced by multiple factors, including diet, genetics, microbiome dynamics, and immune system interactions [43]. Although the exact mechanisms remain partially elucidated, emerging evidence from preclinical models and clinical settings suggests the role of excessive ROS production in the inflamed intestinal tissues of IBD-affected individuals. This overproduction of ROS considerably contributes to oxidative stress and disrupts redox homeostasis, which has been shown to play an essential role in the pathophysiology of IBD. ROS are known to compromise the integrity of the intestinal barrier—a critical component for maintaining gut homeostasis. Damage to this protective epithelial layer results in the exposure of immune cells to intestinal microbes [44], which may further exacerbate the inflammatory response and promote disease progression [45]. Consequently, therapeutic approaches that effectively attenuate ROS levels are increasingly recognized as potential strategies for alleviating the debilitating symptoms of IBD.

V_C is an essential nutrient and potent natural antioxidant, capable of donating electrons to neutralize free radicals [46]. The reactive hydroxyl group in V_C allows for chemical modification and prodrug development, enabling the resulting prodrugs to self-assemble in aqueous solutions. Additionally, vitamin C not only exhibits potent antioxidant properties but also serves as an essential nutrient for the body, making it a safe option with minimal side effects. Upon oxidation, it will lose electrons and convert to free radicals named semihydroascorbic acid or ascorbyl radicals, which are inactive and relatively stable [47]. These merits make the V_C molecule a promising candidate for treating oxidative stress–related diseases. However, the development of V_C as a therapeutic agent has been hindered by some limitations, such as poor bioavailability, a short plasma half-life, insufficient disease site accumulation following systemic administration (either oral or intravenous), and low potency (necessitating a high dose) [48]. Thus, we employed the PUFAylation technology to develop a V_C self-deliverable nanoplatform by conjugating the V_C molecule with long-chain fatty acids, followed by a subsequent nanoassembly protocol. This approach involved conjugating V_C with long-chain fatty acids to form lipid derivatives that spontaneously assemble into nanoparticles. These

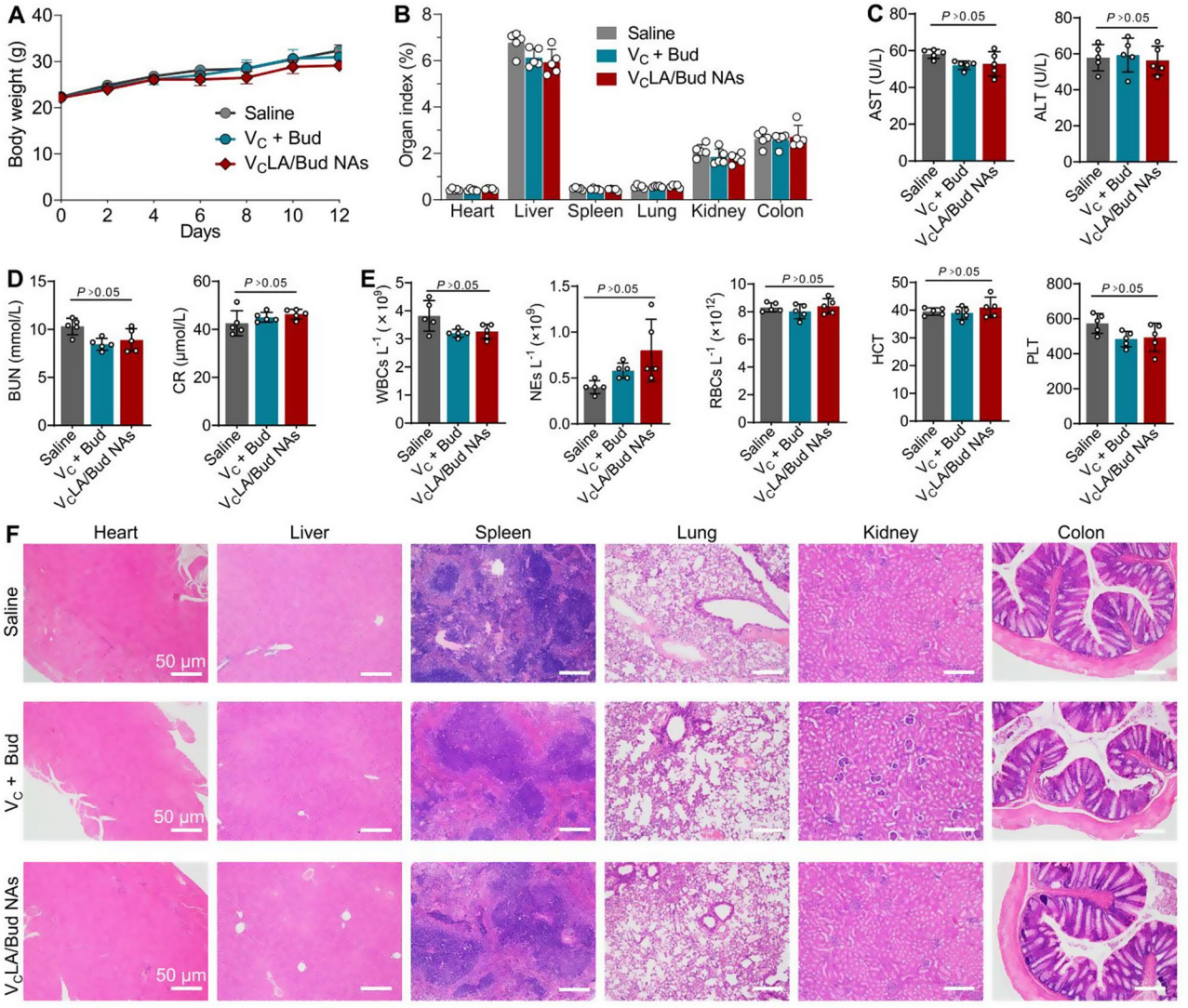

Fig. 8 Safety assessment of V_CLA/Bud nanoassemblies (NAs). Healthy mice were administered saline, a combination of V_C + Bud, or V_CLA/Bud nanoassemblies at twice the therapeutic dose. (**A**) Body weights were recorded every 2 days following the initial dose ($n = 5$). (**B**) Organ indices were calculated by weighing the organs and normalizing them to body weight, indicating no apparent organ enlargement or toxicity ($n = 5$). (**C**-**E**) Serum biochemistry (**C** and **D**) and complete blood count (**E**) and were conducted to evaluate the safety of the treatments ($n = 5$). (**F**) Hematoxylin and eosin (H&E) staining of tissue sections from the heart, liver, spleen, lung, kidney, and colon for morphological analysis. No significant histopathological changes were observed, supporting the high tolerability of V_CLA/Bud nanoassemblies. Data are presented as mean ± standard deviation (s.d.)

nanoassemblies enhanced the bioavailability of V_C, providing a sustained antioxidant effect.

The nanoassembly of V_C–lipid derivatives without needing exogenous excipients enhanced the bioavailability and provided a prolonged therapeutic effect. Particularly, V_CLA nanoassemblies retained the antioxidant activity as ROS scavengers, protecting cells from oxidative stress injury. The lipophilic nature of the nanoassemblies increased their affinity for cell membranes and facilitated endocytosis, leading to a significant reduction in ROS levels and accumulation in the inflamed colon of mice. Therapeutic efficacy was examined in acute and chronic colitis models, with V_CLA nanoassemblies acting as a "nanosweeper" to clear pathologically increased ROS in the inflamed intestinal tissues. Interestingly, the inflammatory microenvironment was modulated, with a decrease in total macrophages and proinflammatory M1-like phenotypes and an increase in anti-inflammatory M2-like phenotypes.

The advantages of this approach are manifold. First, V_C–lipid derivatives released active ingredients through ester hydrolysis in vivo, acting as a drug reservoir for continuous antioxidant provision. Second, the antioxidant and anti-inflammatory properties of PUFAs could amplify the therapeutic effects of V_C, although the effect of PUFAs was not discussed in this study [49].

Furthermore, inflammation-induced enhanced permeability and retention allowed nanoassemblies to passively target inflammatory lesions, increasing delivery efficiency. Finally, the modular assembly strategy enabled the incorporation of additional drug–lipid conjugates, such as Bud, a clinically approved glucocorticoid, into the hybrid nanoplatform, further enhancing IBD therapy compared to a single-drug regimen.

In summary, this work presents a simple and broadly applicable strategy for transforming a poorly druggable natural antioxidant into an effective self-deliverable nanoassembly platform. The potential for preventing and treating acute and chronic inflammation was also investigated using DSS-induced colitis as a mouse model. Given that only two components (i.e., LA and V_C) are released upon hydrolysis of the ester bond, this nanosystem is safe and highly tolerable in vivo. Further preclinical and clinical studies are warranted to assess the long-term safety and therapeutic efficacy of this V_C delivery nanoplatform in various inflammatory diseases.

Materials and methods

Materials

V_C was obtained from Tokyo Chemical Industry (Shanghai, China). Bud was obtained from Macklin Biochemical Co., Ltd. (Shanghai, China). Fatty acids were purchased from Macklin Biochemical Co., Ltd. (Shanghai, China). Lipase was obtained from Sigma-Aldrich (MO, USA). PTIO• was purchased from Tokyo Chemical Industry (Shanghai, China). ABTS+• was purchased from Sigma-Aldrich (MO, USA). DCFH-DA was provided by Beyotime (Shanghai, China). The calcein-AM/PI Double Staining Kit and Cell Counting Kit-8 (CCK-8) were obtained from Dojindo China Co., Ltd. (Shanghai, China).

Antibodies for flow cytometry analysis: BV510-antimouse CD45 (157219, BioLegend), BUV395-antimouse CD11b (565976, BD Biosciences), BV605-antimouse F4/80 (123133, BioLegend), FITC-antimouse CD3 (100203, BioLegend), NUV675-antimouse CD4 (612974, BD Biosciences), BV421-antimouse CD25 (101923, BioLegend), and PE-Cyanine5.5-antimouse FoxP3 (750024, Invitrogen).

Synthesis of V_C–lipid Bud–lipid conjugates

V_C–lipid derivatives were obtained through an esterification reaction catalyzed by lipase. Specifically, V_C (3.52 g, 20 mmol) and fatty acids (e.g., LA, 1.42 g, 5 mmol) were dissolved in 25 mL of anhydrous acetonitrile. Then, lipase (0.30 g) and a molecular sieve were added. The mixture was warmed to 55°C and stirred for 12 h to allow a complete reaction. After the reaction, the solvent is volatilized by rotary evaporation under reduced pressure. Next, silica gel was used as a stationary phase, and a gradient of dichloromethane (DCM) and methanol as eluents was employed for purification by column chromatography to obtain the product. V_C–lipid derivatives were characterized *via* ^{1}H NMR and RP-HPLC. For the preparation of Bud conjugates, Bud (4.31 g, 10 mmol) and LAs (2.80 g, 10 mmol) were mixed in 10 mL of anhydrous DCM. Then 4-dimethylaminopyridine (1.34 g, 11 mmol) and *N*, *N*′-diisopropylcarbodiimide (1.39 g, 11 mmol) were added to the above solution. The mixture was warmed up to 45 °C and stirred for 10 h, and the subsequent purification methods were the same as for V_C–lipid derivatives.

Preparation of carrier-free V_C nanoassemblies

The serial V_C nanoassemblies were prepared using a nanoprecipitation method. Furthermore, 10 mg V_C equivalent V_C–lipid derivatives were dissolved in 0.5 mL of DMSO and then slowly injected into 9.5 mL of DI water under ultrasonic conditions to obtain 1 mg/mL V_C equivalent nanoassemblies. After 5 min of sonication, the nanoassembly solution was transferred to a clean tube and stored at 4 °C for use. With regard to lipo V_C, equivalent V_CLA was dissolved in DMSO and mixed in an ethanol solution containing egg-PC, cholesterol, and DSPE-PEG_{2000} with a mass ratio of 35:5:8 (1 mL, ethanol/DMSO, v/v, 10/1). Next, the above mixture was injected dropwise into 9.0 mL of DI water under magnetic stirring. After that, excess ethanol was evacuated into a fume hood. And then the nanoassemblies were loaded into a 1 kDa molecular weight cutoff dialysis bag. The dialysis bag was then placed in a beaker containing 1 L of deionized (DI) Milli-Q water (Millipore) and stirred for 36 h. During this process, the double-distilled water was replaced three times to ensure the effective removal of DMSO. The final drug concentration was determined using reverse-phase high-performance liquid chromatography (HPLC). For the preparation of V_CLA/Bud nanoassemblies, the V_C conjugates (V_CLA) and Bud conjugates (BudLA) were dissolved in 0.5 mL of DMSO at a mass ratio of 50:1 and then slowly injected into 9.5 mL of DI water to prepare a coassembled nanoparticle solution.

Preparation of VcLA liposomes

VcLA liposomes were prepared by ethanol dilution as described by the previous report [50]. Briefly, the lipid mixture consisting of Egg-PC, cholesterol and DSPE-PEG2k was first dissolved in ethanol (0.9 mL) at a mass ratio of 35:5:8. Next, 0.1 mL of DMSO containing V_CLA (at a concentration of 10 mg/mL, equivalent to V_C) was added to the above ethanolic solution, mataining a lipid-to-VcLA ratio at 25:1 (w/w). The mixture (1 mL) was then rapidly injected into DI water, yielding stable liposomes in water with a concentration of 0.1 mg/mL (V_C-equivalent concentration). Finally, the resulting liposomes were reprecipitated by ultracentrifugation at 100,000 g for

20 min and washed three times with DI water to remove organic solvents. The detailed protocol has been added to the revised Materials and Methods section.

Evaluation of free radical–scavenging ability in vitro

PTIO• and ABTS+• free radicals were employed to evaluate the in vitro free radical–scavenging capacity of V_C–lipid derivatives. The elimination of PTIO• free radicals was determined by incubating V_C or V_C–lipid derivatives (at concentrations ranging from 12.5 to 800 μg/mL VC equivalent) with PTIO• (1 mM) in the dark for 2 h at room temperature, followed by measurement of absorbance at 557 nm using a multimode microplate reader. ABTS+• elimination was assessed by incubating V_C or V_CLA nanocomponents (at concentrations ranging from 12.5 to 800 μg/mL V_C equivalent) with ABTS+• (0.1 mM) for 10 min in the dark at room temperature and measuring absorbance at a wavelength of 415 nm using a multimode microplate reader.

Cell lines and cell culture

The mouse macrophage–like cell line RAW264.7 and the normal-derived human colon mucosa cell line NCM460 were purchased from the cell bank of the Chinese Academy of Sciences (Shanghai, China). RAW264.7 was cultured in alexin-free DMEM, while NCM460 was cultured in DMEM/F12. All media were supplemented with 100 units/mL penicillin, 100 μg/mL streptomycin, and 10% fetal bovine serum (FBS). Cells were cultured at 37 °C, containing 5% carbon dioxide.

Measurement of ROS in cell lines

RAW264.7 was seeded into sterile 48-well plates at a density of 4×10^4 cells per well and cultured for 12 h. Subsequently, they were treated with various V_C formulations, including V_C + LPS and V_CLA NAs + LPS, both at a concentration of 100 μM V_C equivalent and 1 μg/mL LPS. PBS was used as a negative control, while 1 μg/mL LPS served as a positive control. Following 6 h of incubation, the existing solution was removed, and DCFH-DA was added to detect the generation of ROS, while Hoechst 33,342 was utilized to stain the nuclei. Next, the fluorescence microscope was used to observe the fluorescence intensity and record the images.

Calcein-AM/PI staining

For the H_2O_2 removal experiment, RAW264.7 or NCM460 were seeded into sterile 48-well plates at a density of 2×10^4 cells per well and cultured for 12 h. Subsequently, they were treated with different V_C formulations, including V_C + H_2O_2 and V_CLA NAs + H_2O_2, at various concentrations of V_C equivalent (12.5, 25, and 50 μM) and 600 mM H_2O_2. PBS was used as a negative control, while 600 mM H_2O_2 served as a positive control. Following 4 h of incubation, the cells were stained with calcein-AM/PI and imaged using fluorescence microscopy.

CCK-8 assay

CCK-8 was employed to detect cell viability following treatment with different H_2O_2 formulations. Briefly, RAW264.7 or NCM460 were seeded into sterile 96-well plates at a density of 2×10^4 cells per well. After 12 h of incubation, the medium was refreshed, and then RAW264.7 was treated with various concentrations of V_C or V_CLA nanoassemblies and a fixed concentration of H_2O_2 (600 mM). While NCM460 was treated with V_C or V_CLA nanoassemblies (at a V_C equivalent concentration of 50 μM) together with an increasing concentration of H_2O_2. After incubating for 6 h, cell viability was measured using the CCK-8 assay.

Animal experiments

Animals were purchased from the Laboratory Animal Center of Hangzhou Medical College (Hangzhou, China). All animal studies complied with the National Laboratory Animal Care and Use Institute guidelines. The animals involved in the experiment were reviewed and approved by the Ethics Committee of the First Affiliated Hospital, School of Medicine, Zhejiang University.

Determination of in vivo anti-ROS ability

The in vivo anti-ROS efficacy of V_CLA nanoassemblies was evaluated using the commercial ROS probe L-012. Six week–old C57BL/6 mice were administered water containing 3% DSS for one week to induce colitis. Initially, L-012 was intraperitoneally injected at a dose of 25 mg/kg for NIRF imaging, with the fluorescence intensity serving as the baseline value. Then, mice were treated with saline, V_C, or V_CLA nanoassemblies (at a V_C equivalent dose of 30 mg/kg) via intraperitoneal injection ($n = 4$–5). After 6 h of treatment, the same dose of L-012 was administered again for NIRF imaging, with fluorescence intensity serving as the post-treatment value.

Assessment of in vivo accumulation capacity of V_CLA nanoassemblies

The synthesis method for Cy5.5 conjugates (Cy5.5LA) remained consistent with that of the previous study [51]. Briefly, Cy5.5 amine (12.8 mg, 0.017 mmol) and LA (5.8 mg, 0.020 mmol) were dissolved in 3 mL of DCM. Furthermore, EDC (2.4 mg, 0.020 mmol) and DMAP (3.2 mg, 0.020 mmol) were added to this solution. The resulting mixture was stirred at 45°C for 3 h. Following solvent removal, DCM was introduced and subjected to sequential washes with 5% citric acid, a saturated sodium bicarbonate solution, and brine. The organic layer was dried over anhydrous sodium sulfate, filtered, and subsequently evaporated under vacuum. The resulting residue

was purified using flash column chromatography on silica gel, utilizing a mixture of DCM and methanol in a ratio of 20:1, yielding Cy5.5LA.

For the preparation of Cy5.5-labeled V_CLA nanoassemblies, V_CLA and Cy5.5LA were dissolved in 0.5 mL of DMSO and slowly injected into 9.5 mL of DI water to prepare a coassembled nanoparticle solution, achieving a final concentration of 1 mg/mL V_C equivalence and 50 μg/mL Cy5.5 equivalence. The procedure for inducing colitis followed the same protocol described above, with a group receiving fresh water as a healthy control ($n = 4$). After colitis induction, mice were intraperitoneally administered 200 μL of Cy5.5-labeled V_CLA nanoassemblies. After 6 h, mice were euthanized to collect hearts, livers, spleens, lungs, kidneys, and colons for NIRF imaging.

In vivo antioxidant activity in acute colitis

The modeling process of acute colitis followed the same procedure described above, while another group was given fresh water as a healthy control ($n = 5$). Notably, mice were intraperitoneally injected with saline, V_C, V_CLA liposome, or V_CLA nanoassemblies at a dose of 10 mg/kg (V_C equivalent) every day for a total of seven injections. The body weights of mice were recorded daily. The feces of each mouse were collected for the DAI score and fecal occult blood test via fecal occult blood test paper on day 6. At the end of the experiment, mice were euthanized, and their spleens were harvested for weighing. Additionally, colon lengths were measured after washing off the feces.

In vivo antioxidant activity in chronic colitis

A chronic colitis mouse model was induced by administering water containing 3.5% DSS intermittently, alternating with periods of fresh water. A healthy control group received only fresh water ($n = 5$). Subsequently, mice were treated with saline, BudLA nanoassemblies, V_CLA nanoassemblies, or V_CLA/Bud nanoassemblies at a dosage of 10 mg/kg V_C equivalent and 0.2 mg/kg Bud equivalent from day 15 to day 30 ($n = 5$). Throughout the study, the body weights and survival rates of mice were monitored. Feces were collected for DAI assessment and fecal occult blood testing as described above. After euthanasia, the spleens and colons were harvested for weight or length measurements.

Inflammatory microenvironment analysis

Cytokine assays and immune profiling were performed using a chronic colitis model induced by administering 3.5% DSS in drinking water from days 0 to 5 and days 15 to 20, alternating with fresh water from days 5 to 15 and days 20 to 25. The healthy control group received only fresh water throughout the experiment period. Starting on day 15, mice were treated once daily with saline, BudLA nanoassemblies, V_CLA nanoassemblies, or V_CLA/Bud nanoassemblies at doses equivalent to 10 mg/kg of V_C and 0.2 mg/kg of Bud. Samples were collected on day 25 for further analysis.

Colons were excised and immersed in a cold Hank's Balanced Salt Solution (HBSS, devoid of Ca^{2+} and Mg^{2+}). After trimming their mesenteries, the colons were longitudinally opened, extensively washed with HBSS, and then divided into small fragments. The dissected tissue was subsequently placed in HBSS containing DTT (1 mM) and EDTA (5 mM) and incubated at 37 °C for 0.5 h to remove the epithelial layer. After washing, the tissue segments were incubated in HBSS containing 1.5% FBS, collagenase III (200 U/mL), and DNase I (0.01 mg/mL) for 1 h at 37 °C to facilitate digestion. Afterward, the tissue was passed through a 70-μm filter to obtain single-cell suspensions. These cells were then suspended in Percoll, followed by centrifugation at 750 g for 20 min at room temperature for Percoll gradient separation to isolate intestinal lamina propria cells. Subsequently, antibodies were used to stain lamina propria cells for flow cytometry analysis as follows: anti-CD45 (BV510), anti-CD11b (BUV395), anti-F4/80 (BV605), anti-CD86 (PE), anti-CD206 (APC), anti-CD3 (FITC), anti-CD4 (NUV675), anti-CD25 (BV421), and anti-FoxP3 (PE-Cyanine5.5). To determine inflammatory cytokines, the Mouse Inflammation Panel (Biolegend, USA) was applied to measure the pathological changes of inflammatory factors in mice serum.

Microbiome analysis

Fecal samples were carefully collected from each mouse. Fecal samples were properly packaged and sent to Sangon Biotech (Shanghai) Co., Ltd. for microbiome analysis. In short, genomic DNA extraction was performed using an EZNA™ MagBind Soil DNA Kit (Omega, M5635-02, USA), following the manufacturer's instructions. The resulting DNA was then used to construct 16 S rRNA libraries for community analysis on the Illumina MiSeq sequencing platform (Illumina MiSeq, USA). In particular, barcoded dual-index primers designed for the V3–V4 region of the 16 S rRNA gene were used for constructing libraries. Following sequencing, the resulting short Illumina reads were assembled using PEAR software (version 0.9.8) based on overlap. The FASTQ files were subsequently processed to produce separate FASTA and QUAL files, which were then subjected to analysis using standard methods. The valid tags were grouped into operational taxonomic units (OTUs) with a similarity of ≥97% using Usearch software (version 11.0.667). Chimeric sequences and singleton OTUs (those with only one read) were eliminated. Subsequently, the remaining sequences were assigned to each sample based on the

OTUs. The most abundant tag sequences were chosen as representative sequences within each cluster. Additionally, representative sequences of bacterial and fungal OTUs were classified using the control RDP database and the combined fungal ITS database, respectively.

Histological analysis of colon tissues

Histological analysis of colonic tissues was performed using hematoxylin and eosin (H&E), Masson's trichrome, and periodic acid–Schiff (PAS) staining. Colons were fixed in formalin and embedded in paraffin.

For H&E staining, tissue sections were stained with hematoxylin for 5 min, followed by differentiation in aqueous hydrochloric acid solution for 2 s. Then, the slides were treated with aqueous ammonia solution for 15–30 s and rinsed in distilled water. Next, the sections were dehydrated in 95% ethanol and stained with eosin for 5–8 s. After mounting the sections with neutral gum, images were acquired and analyzed using microscopy.

Masson's trichrome staining was employed to visualize collagen fibers in colon tissues. Briefly, paraffin-embedded colon tissues were sectioned, dewaxed with xylene, and rehydrated through a graded ethanol series. Sections were stained with hematoxylin for 8 min, followed by Biebrich scarlet–acid fuchsin staining for 10 min. After been treated phosphotungstic/phosphomolybdic acid for 10 min, the sections were directly transferred into aniline blue for 5 min. Following dehydration with a graded ethanol series and mounting with neutral gum, the stained sections were observed under an optical microscope.

PAS staining was performed to detect mucopolysaccharides and glycogen in colonic tissues. After dewaxing and rehydration, sections were oxidized in 0.5% periodic acid solution for 10 min, rinsed in distilled water, and stained with Schiff's reagent for 10–15 min. The slides were then washed in running water for 5 min, counterstained with hematoxylin for 1–2 min, and rinsed in distilled water. Finally, the sections were dehydrated through a graded ethanol series, cleared in xylene, mounted with neutral gum, and imaged using an optical microscope.

Immunofluorescence imaging

Immunofluorescence imaging was performed to visualize specific protein expression in colonic tissues. Paraffin-embedded tissue sections were deparaffinized in xylene and rehydrated through a graded ethanol series. Antigen retrieval was carried out by incubating sections in citrate buffer (pH 6.0) at 95 °C for 15 min, followed by gradual cooling to room temperature. After three washes with phosphate-buffered saline (PBS), sections were blocked with 5% bovine serum albumin (BSA) for 1 h at room temperature to prevent non-specific binding.

Primary antibodies specific to the target proteins were diluted in PBS containing 1% BSA and incubated with the sections overnight at 4°C in a humidified chamber. After washing three times with PBS, sections were incubated with fluorophore-conjugated secondary antibodies at room temperature for 1 hour in the dark. To visualize nuclei, sections were counterstained with 4',6-diamidino-2-phenylindole (DAPI) for 5 min.

After final PBS washes, sections were mounted with antifade fluorescence mounting medium and sealed with coverslips. Fluorescence images were acquired using a confocal laser scanning microscope, with excitation and emission wavelengths set according to the fluorophores used. Image analysis was conducted using ImageJ software.

Safety study in mice

The safety of V_CLA/Bud nanoassemblies in healthy ICR mice was investigated. Mice were given daily intraperitoneal injections of saline, V_C + Bud (a mixture of V_C and Bud solution), or V_CLA/Bud nanoassemblies at a dosage of 20 mg/kg V_C equivalent and 0.2 mg/kg Bud equivalent from day 0 to day 6. Body weight was measured every other day. On day 12, mice were euthanized, and organs were weighed. Additionally, blood samples were collected from mice for a complete blood count and blood biochemistry tests.

Statistical analysis

Statistical analyses were conducted with Prism software version 10.0 (GraphPad). Data were expressed as mean ± standard deviation (s.d.). The unpaired Student's *t*-test was used to assess statistical significance. Furthermore, survival studies were analyzed using Kaplan–Meier plots.

Supplementary Information

The online version contains supplementary material available at https://doi.org/10.1186/s12951-025-03322-0.

Supplementary Material 1

Acknowledgements

We thank Lingyun Wu from the Center of Cryo-Electron Microscopy (CCEM), Zhejiang University, for the technical assistance with Cryo-transmission electron microscope analysis. We thank Yanwei Li and Chun Guo from the Core Facilities, Zhejiang University School of medicine for their technical support.

Author contributions

S. X. conducted most of the experiments and wrote the draft of manuscript. F. M. verified the underlying data. X. C. assisted with the experiment. L. Z. validated the data and H. W. designed the study and critically revised the work. All authors read and approved the final manuscript.

Funding

This work was supported by grants from Natural Science Foundation of Shandong Province (ZR2023ZD59), "Pioneer" and "Leading Goose" R&D Program of Zhejiang Province (2025C01217), National Natural Science Foundation of China (82273490, 82073296 and 82272784), Non-profit Central Research Institute Fund of Chinese Academy of Medical Sciences (2023-

PT320-02), Research Project of Jinan Microecological Biomedicine Shandong Laboratory (JNL-2022010B and JNL-2025007B), and Beijing Natural Science foundation (7252006).

Data availability
No datasets were generated or analysed during the current study.

Declarations

Ethics approval and consent to participate
All animal procedures were performed following protocols approved by the Ethics Committee of the First Affiliated Hospital, School of Medicine, Zhejiang University. All animal studies complied with the National Laboratory Animal Care and Use Institute guidelines.

Consent for publication
Consents for publication were obtained from all the authors of this study.

Competing interests
The authors declare no competing interests.

Received: 11 November 2024 / Accepted: 11 March 2025
Published online: 25 March 2025

References

1. Ramos GP, Papadakis KA. Mechanisms of disease: inflammatory bowel diseases. In *Mayo Clinic Proceedings*. Elsevier; 2019: 155–165.
2. Ananthakrishnan AN, Kaplan GG, Ng SC. Changing global epidemiology of inflammatory bowel diseases: sustaining health care delivery into the 21st century. Clin Gastroenterol Hepatol. 2020;18:1252–60.
3. Itzkowitz SH, Yio X. Inflammation and cancer IV. Colorectal cancer in inflammatory bowel disease: the role of inflammation. Am J Physiol Gastrointest Liver Physiol. 2004;287:G7–17.
4. Han W, Xie B, Li Y, Shi L, Wan J, Chen X, Wang H. Orally deliverable nanotherapeutics for the synergistic treatment of Colitis-Associated colorectal cancer. Theranostics. 2019;9:7458–73.
5. de Mattos BR, Garcia MP, Nogueira JB, Paiatto LN, Albuquerque CG, Souza CL, Fernandes LG, Tamashiro WM, Simioni PU. Inflammatory Bowel Disease: An Overview of Immune Mechanisms and Biological Treatments. *Mediators Inflamm* 2015, 2015:493012.
6. Tian T, Wang Z, Zhang J. Pathomechanisms of oxidative stress in inflammatory bowel disease and potential antioxidant therapies. Oxid Med Cell Longev. 2017;2017:4535194.
7. Zhang C, Wang H, Yang X, Fu Z, Ji X, Shi Y, Zhong J, Hu W, Ye Y, Wang Z, Ni D. Oral zero-valent-molybdenum nanodots for inflammatory bowel disease therapy. Sci Adv. 2022;8:eabp9882.
8. Dagli U, Balk M, Yücel D, Ulker A, Over H, Saydam G, Sahin B. The role of reactive oxygen metabolites in ulcerative colitis. Inflamm Bowel Dis. 1997;3:260–4.
9. Grebe M, Eisele HJ, Weissmann N, Schaefer C, Tillmanns H, Seeger W, Schulz R. Antioxidant vitamin C improves endothelial function in obstructive sleep apnea. Am J Respir Crit Care Med. 2006;173:897–901.
10. Padayatty SJ, Katz A, Wang Y, Eck P, Kwon O, Lee JH, Chen S, Corpe C, Dutta A, Dutta SK, Levine M. Vitamin C as an antioxidant: evaluation of its role in disease prevention. J Am Coll Nutr. 2003;22:18–35.
11. Lykkesfeldt J, Tveden-Nyborg PJN. The pharmacokinetics of vitamin C. 2019, 11:2412.
12. Padayatty SJ, Sun H, Wang Y, Riordan HD, Hewitt SM, Katz A, Wesley RA, Levine M. Vitamin C pharmacokinetics: implications for oral and intravenous use. Ann Intern Med. 2004;140:533–7.
13. Wang H, Lu Z, Wang L, Guo T, Wu J, Wan J, Zhou L, Li H, Li Z, Jiang D, et al. New generation nanomedicines constructed from Self-Assembling Small-Molecule prodrugs alleviate cancer drug toxicity. Cancer Res. 2017;77:6963–74.
14. Xian S, Chen X, Ren S, Chen X, Wang H. Ionizable STING-Activating nanoadjuvants enhance tumor immunogenicity and potentiate immunotherapy efficacy in solid tumors. Cancer Res. 2024;84:3044–57.
15. Chen X, Meng F, Xu Y, Li T, Chen X, Wang H. Chemically programmed STING-activating nano-liposomal vesicles improve anticancer immunity. Nat Commun. 2023;14:4584.
16. Bian S, Dong H, Zhao L, Li Z, Chen J, Zhu X, Qiu N, Jia X, Song W, Li Z, et al. Antihypertension nanoblockers increase intratumoral perfusion of sequential cytotoxic nanoparticles to enhance chemotherapy efficacy against pancreatic cancer. Adv Sci (Weinh). 2022;9:e2201931.
17. Ren L, Wan J, Li X, Yao J, Ma Y, Meng F, Zheng S, Han W, Wang H. Mitochondrial rewiring with small-molecule drug-free nanoassemblies unleashes anticancer immunity. Nat Commun. 2024;15:7664.
18. Shahidi F. Ambigaipalan PJArofs, technology: Omega-3 polyunsaturated fatty acids and their health benefits. 2018, 9:345–381.
19. Wu L, Zhang F, Chen X, Wan J, Wang Y, Li T, Wang H. Self-Assembled gemcitabine prodrug nanoparticles show enhanced efficacy against Patient-Derived pancreatic ductal adenocarcinoma. ACS Appl Mater Interfaces. 2020;12:3327–40.
20. Guo J, Wang F, Hu Y, Luo Y, Wei Y, Xu K, Zhang H, Liu H, Bo L, Lv S, et al. Exosome-based bone-targeting drug delivery alleviates impaired osteoblastic bone formation and bone loss in inflammatory bowel diseases. Cell Rep Med. 2023;4:100881.
21. Zhang R, Qin X, Kong F, Chen P, Pan GJDD. Improving cellular uptake of therapeutic entities through interaction with components of cell membrane. 2019, 26:328–42.
22. Fakhoury M, Negrulj R, Mooranian A. Al-Salami HJJoir: Inflammatory bowel disease: clinical aspects and treatments. 2014:113–120.
23. Bhattacharyya A, Chattopadhyay R, Mitra S, Crowe SEJP. Oxidative stress: an essential factor in the pathogenesis of Gastrointestinal mucosal diseases. 2014, 94:329–54.
24. Rao RJF. Library V: oxidative stress-induced disruption of epithelial and endothelial tight junctions. 2008, 13:7210.
25. Park J-I, Seo S-M, Park J-H, Jeon H-Y, Kim J-Y, Ryu S-H. Choi Y-KJjom: A murine colitis model developed using a combination of dextran sulfate sodium and citrobacter rodentium. 2018, 56:272–9.
26. Xie J, Itzkowitz SHJWW. Cancer in inflammatory bowel disease. 2008, 14:378.
27. Silverman J, Otley AJERCI. Budesonide in the treatment of inflammatory bowel disease. 2011, 7:419–428.
28. Bruscoli S, Febo M, Riccardi C, Migliorati GJF. Glucocorticoid therapy in inflammatory bowel disease: mechanisms and clinical practice. 2021, 12:691480.
29. Xian S, Zhu J, Wang Y, Song H, Wang H. Oral liposomal delivery of an activatable Budesonide prodrug reduces colitis in experimental mice. Drug Deliv. 2023;30:2183821.
30. Lee BC, Lee JY, Kim J, Yoo JM, Kang I, Kim JJ, Shin N, Kim DJ, Choi SW, Kim D, et al. Graphene quantum Dots as anti-inflammatory therapy for colitis. Sci Adv. 2020;6:eaaz2630.
31. Neurath MFJNRI. Cytokines in inflammatory bowel disease. 2014, 14:329–342.
32. Lopetuso LR, Chowdhry S, Pizarro TTJF. Opposing functions of classic and novel IL-1 family members in gut health and disease. 2013, 4:181.
33. Ohman L, Dahlén R, Isaksson S, Sjöling A, Wick MJ, Sjövall H, Van Oudenhove L, Simrén M, Strid H. Serum IL-17A in newly diagnosed treatment-naive patients with ulcerative colitis reflects clinical disease severity and predicts the course of disease. Inflamm Bowel Dis. 2013;19:2433–9.
34. Becher B, Tugues S, Greter MJI. GM-CSF: from growth factor to central mediator of tissue inflammation. 2016, 45:963–73.
35. Zheng X, Jiang Q, Han M, Ye F, Wang M, Qiu Y, Wang J, Gao M, Hou F, Wang H. FBXO38 regulates macrophage polarization to control the development of cancer and colitis. Cell Mol Immunol. 2023;20:1367–78.
36. Ohue Y, Nishikawa HJC. Regulatory T (Treg) cells in cancer: can Treg cells be a new therapeutic target? 2019, 110:2080–9.
37. Round JL, Mazmanian SK. The gut microbiota shapes intestinal immune responses during health and disease. Nat Rev Immunol. 2009;9:313–23.
38. Kostic AD, Xavier RJ, Gevers D. The Microbiome in inflammatory bowel disease: current status and the future ahead. Gastroenterology. 2014;146:1489–99.
39. Cani PD, de Vos WM. Next-Generation beneficial microbes: the case of Akkermansia muciniphila. Front Microbiol. 2017;8:1765.
40. Everard A, Belzer C, Geurts L, Ouwerkerk JP, Druart C, Bindels LB, Guiot Y, Derrien M, Muccioli GG, Delzenne NM, et al. Cross-talk between Akkermansia muciniphila and intestinal epithelium controls diet-induced obesity. Proc Natl Acad Sci U S A. 2013;110:9066–71.
41. Zhang Z, Wu X, Cao S, Cromie M, Shen Y, Feng Y, Yang H, Li L. Chlorogenic acid ameliorates experimental colitis by promoting growth of Akkermansia in mice. Nutrients 2017, 9.

42. Geirnaert A, Calatayud M, Grootaert C, Laukens D, Devriese S, Smagghe G, De Vos M, Boon N, Van de Wiele T. Butyrate-producing bacteria supplemented in vitro to Crohn's disease patient microbiota increased butyrate production and enhanced intestinal epithelial barrier integrity. Sci Rep. 2017;7:11450.
43. Loddo I, Romano CJF. Inflammatory bowel disease: genetics, epigenetics, and pathogenesis. 2015, 6:159896.
44. Aviello G. Knaus UJBjop: ROS in Gastrointestinal inflammation: rescue or sabotage? 2017, 174:1704–18.
45. Zhu H, Li YRJEB, Medicine. Oxidative stress and redox signaling mechanisms of inflammatory bowel disease: updated experimental and clinical evidence. 2012, 237:474–80.
46. Berger MM. Vitamin C requirements in parenteral nutrition. Gastroenterology. 2009;137:S70–78.
47. Kiokias S, Varzakas TH, Arvanitoyannis IS. Labropoulos AEJAifb: 12 Lipid Oxidation and Control of Oxidation. 2010:383.
48. Doseděl M, Jirkovský E, Macáková K, Krčmová LK, Javorská L, Pourová J, Mercolini L, Remião F, Nováková L, Mladěnka PJN. Vitamin C—sources, physiological role, kinetics, deficiency, use, toxicity, and determination. 2021, 13:615.
49. Delmastro-Greenwood M, Freeman BA, Wendell, SGJArop. Redox-dependent anti-inflammatory signaling actions of unsaturated fatty acids. 2014, 76:79–105.
50. Fang T, Dong Y, Zhang X, Xie K, Lin L, Wang H. Integrating a novel SN38 prodrug into the pegylated liposomal system as a robust platform for efficient cancer therapy in solid tumors. Int J Pharm. 2016;512:39–48.
51. Xie H, Zhu H, Zhou K, Wan J, Zhang L, Yang Z, Zhou L, Chen X, Xu X, Zheng S, Wang H. Target-oriented delivery of self-assembled immunosuppressant cocktails prolongs allogeneic orthotopic liver transplant survival. J Control Release. 2020;328:237–50.

Publisher's note